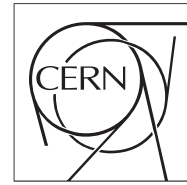


The Compact Muon Solenoid Experiment
Conference Report

Mailing address: CMS CERN, CH-1211 GENEVA 23, Switzerland



28 July 2009 (v3, 28 September 2009)

Electron and photon reconstruction in CMS

Pascal Vanlaer

Université Libre de Bruxelles, Interuniversity Institute for High Energies (IIHE-ULB)

on behalf of the CMS Collaboration.

Abstract

The CMS electromagnetic calorimeter (ECAL) is described as well as its expected performance and recent ECAL commissioning results. Electron and photon reconstruction are then described, starting from the reconstruction of energy deposits in the ECAL by energy clustering algorithms, then proceeding with electron tracking. Electron and photon selection are described. The commissioning of electron and photon physics objects from the measurement of electroweak processes is also shown.

Presented at IPM09: 1st IPM Meeting On LHC Physics

1 The CMS Electromagnetic Calorimeter ECAL

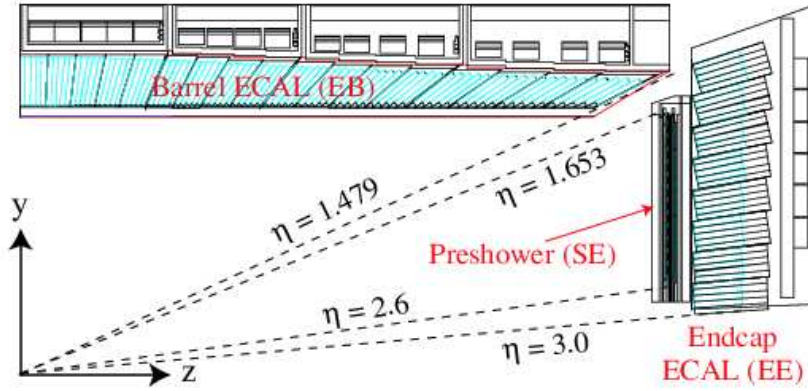


Figure 1: Longitudinal view of one quarter of the ECAL [2].

The CMS electromagnetic calorimeter ECAL and its performance are presented in Refs. [1, 2]. The ECAL is divided in a barrel section (EB) and two endcaps (EE), as shown in Fig. 1. The excellent linearity between the energy deposited by electromagnetic showers and the measured electronics signals, as determined through calibration procedures, is expected to lead to an energy resolution given by a quadratic sum of terms: $\sigma/E = 0.55\% \oplus 2.7\%/\sqrt{E} \oplus 0.155/E$ in EB for $\eta = 0$, and $\sigma/E = 0.55\% \oplus 5.7\%/\sqrt{E} \oplus 0.205/E$ in EE for $\eta = 2$, with E in GeV [2]. At high energy, the constant term dominates, and the energy resolution is expected to be $\simeq 0.6\%$.

1.1 ECAL geometry

The ECAL consists of 75848 PbWO_4 crystals, with density $\rho = 8.3 \text{ g/cm}^3$, radiation length $X_0 = 0.89 \text{ cm}$ and Moliere radius $r_M = 2.19 \text{ cm}$. The crystals are positioned according to a quasi-projective geometry toward the nominal interaction point, with additional off-pointings intended at reducing the effects of cracks. The off-pointings are of 3° both in the azimuthal (ϕ) and the polar (θ) directions for the barrel, and of 3° in ϕ and between 2 to 8° in θ for the endcaps.

The barrel covers the rapidity region $|\eta| < 1.479$ ($\theta = 25.6^\circ$). It is divided in two halves, consisting of 18 supermodules, each of which covers 20° in ϕ . Each supermodule is divided in four modules, and each module is composed of glass-fiber alveola structures called sub-modules, housing 5×2 crystals in $\eta \times \phi$. The $\eta \times \phi$ extension of the modules is of 4×4 trigger towers of 5×5 crystals (5×4 towers for the first module). The gaps between modules are of $\sim 6 \text{ mm}$ in both η and ϕ . The 61200 EB crystals have truncated pyramidal shapes (17 types in total to ensure complete coverage) with (approximately) squared $\sim 2.2 \times 2.2 \text{ cm}^2$ front faces, which corresponds to widths in ϕ of $\sim 1^\circ \simeq 0.0174 \text{ rad}$ and in η of ~ 0.0174 , nearly constant over the whole EB length. The crystal lateral extensions thus correspond to about $1 r_M$. The crystal length in the EB is 230 mm , i.e. $25.8 X_0$. The centres of the crystal front faces are lying at a radius $R = 1.29 \text{ m}$ of the beam axis.

The endcaps, situated at 3.21 m of the nominal interaction point, extend the angular coverage to $|\eta| < 3.0$ ($\theta = 5.7^\circ$). Each endcap is made of two D-shaped structures, where the crystals are distributed in a $x-y$ grid. The 14648 EE crystals have a nearly parallelepipedic shape, with $\sim 2.9 \times 2.9 \text{ cm}^2$ front faces and length 220 mm , i.e. $24.7 X_0$. In front of most of the endcaps, a Pb-Si preshower covers $1.653 \leq |\eta| \leq 2.6$ (i.e. radii $123 \text{ cm} \geq R \geq 45 \text{ cm}$ from the beam axis). Its thickness corresponds to $3 X_0$.

The ECAL calorimeter is surrounding the tracker, and is inserted into the hadronic calorimeter HCAL. The material budget in front of the ECAL crystals, due to beam pipe, tracker, cables and supports, varies with η from a minimum of $0.4 X_0$ at $\eta = 0$ to a maximum of $1.7 X_0$ for $|\eta| \simeq 1.4$, with $1 X_0$ for $|\eta| = 2.5$ [1].

1.2 PbWO_4 scintillating crystals

The characteristics of the PbWO_4 crystals make them an appropriate choice for operation at LHC. The high density, short radiation length and small Moliere radius make a fine granularity, compact calorimeter possible. An electromagnetic shower of 100 GeV is essentially fully contained in length. The small Moliere radius makes it

such that a 5×5 crystal matrix in the barrel (resp. in the endcaps) contains 96.5% (resp. 97.5%) of the energy of an incident unconverted photon.

The scintillation decay time of CMS crystals is of the same order of magnitude as the LHC bunch crossing time: about 80% of the light is emitted in 25 ns. The light output is relatively low: at 18°C about 4.5 photoelectrons per MeV are collected in the photoamplifiers (APDs in the barrel and VPTs in the endcaps). The crystals emit blue-green scintillation light with a broad maximum at 420-430 nm. The light yield of the crystals varies with temperature ($-2\%/^{\circ}\text{C}$ at 18°C) and so does the gain of the barrel APDs ($-2.3\%/^{\circ}\text{C}$) [4]. The crystal and photoamplifier temperature is thus required to be stabilized to 50 millidegrees in the barrel (0.1 degree in the endcaps) so that temperature fluctuations have a negligible contribution to the ECAL energy resolution. Temperature stability well within specifications was demonstrated in an extended one-month data taking period in cosmic rays in october-november 2008, during which the CMS magnetic field was kept at its nominal value of 3.8 Tesla (Cosmic Ray test At Four Tesla - CRAFT08) [4].

An important constraint is the radiation environment. The dose expected is 4 kGy at shower maximum in the ECAL barrel, 90 kGy at $|\eta| = 2.6$, 200 kGy at $|\eta| = 3$. The permanent damage to crystals was tested to be such that the scintillation light attenuation length remains longer than three times the crystal length. The irradiation also results in a transient, dose-rate dependent light attenuation. The dose rate expected at high LHC luminosity is 0.3 Gy/h at shower maximum in the barrel, 6.5 Gy/h at $|\eta| = 2.6$ and 15 Gy/h at $|\eta| = 3$. In the varying conditions of LHC running the result is a cyclic transparency behaviour between LHC collision runs and machine refills. The magnitude of the changes is dose-rate dependent, and is expected to range from 1 or 2 per cent at low luminosity in the barrel, to tens of per cent in the high η regions of the endcap at high luminosity. Under continuous irradiation the time to reach a constant light yield amounts to about 1 day [3].

To achieve design energy resolution the evolution of the crystal transparency must be monitored continuously. This monitoring is performed using laser pulses injected into the crystals via optical fibres. The response is normalized by the laser pulse magnitude measured using silicon PN photodiodes. Thus $R(t) = \frac{APD(t)}{PN(t)}$ is used as the measure of the crystal transparency. Because of the different optical paths and spectra of the injected laser pulses and the scintillation light, the changes in crystal transparency cause a change in response to the laser light which is not necessarily equal to the change in response to scintillation light. For attenuations $< 10\%$ the relationship between the changes can be expressed by a power law,

$$\frac{S(t)}{S(t_0)} = \left(\frac{R(t)}{R(t_0)} \right)^{\alpha}$$

where $S(t)$ represents the response to scintillation light and $\alpha \simeq 1.6$ is a characteristic of the production process and can be determined using data. This power law describes well the behaviour of all the crystals that have been evaluated in the test beam, and this formula is expected to be valid in the barrel for both low and high luminosity at LHC. The entire ECAL is scanned every 30 minutes.

The stability of the laser monitoring system was tested in absence of irradiation during CRAFT08. In nominal data taking conditions, a stability better than the required performance (0.2%) was measured for a period of 1 week [4].

1.3 Photoamplifiers

The barrel crystal scintillation light are readout by a pair of Avalanche PhotoDiodes (APDs) operated at a gain of 50. Since the APD gain has a high dependence on the bias voltage ($\alpha_V = 1/M.dM/dV \simeq 3\%/V$ at gain 50), to keep this contribution to the resolution at the level of per mille, the APDs require a very stable power supply system: the stability of the voltage has to be of the order of few tens of mV. A stability of 2.1 mV RMS, and below 10 mV for all channels, was recorded during CRAFT08 [4].

In the endcaps, Vacuum PhotoTriodes (VPTs) are used and operated at a gain of 10. The spread in response among the VPTs is 25% (RMS). They are therefore sorted into six groups which are distributed on the endcaps with the highest sensitivities at the outer circumference grading to the lowest sensitivities at the inner circumference. This arrangement provides a roughly constant sensitivity to the transverse energy across the endcaps.

2 Energy reconstruction

About 96.5% of the shower of an incident unconverted photon is contained in a matrix of 5×5 crystals in $\eta \times \phi$ in Module 1 of the ECAL barrel. This fraction is measured in test beams with electrons, in the absence of tracker material in front of the crystals and in the absence of magnetic field.

In the experiment, electrons will emit Bremsstrahlung photons in the tracker material, and an important fraction of the photons will convert. Their energy will be spread in ϕ because of the magnetic field. Hit crystals belonging to the same shower are grouped together in clusters and their energy is summed (**superclustering**). For this sum to be a precise measurement of the electron or photon energy at the primary vertex, a number of calibrations and energy corrections have to be performed:

- the uniformization of the response of the different crystals to a fixed incident energy, or **crystal-to-crystal intercalibration**;
- the **corrections** applied to the supercluster energy, for the non-uniform energy loss in η due to the quasi-pointing geometry of the crystals in the ECAL barrel and due to tracker material, for the non-uniformity due to intermodule cracks, and the small difference in containment dependent on the position of the particle impact point within a crystal. In spite of the very good linearity of the ECAL response, small residual dependences in the transverse energy E_T due to material effects and rear leakage at very high energy are expected, which also have to be corrected for;
- the **scale determination**, i.e. the global constant factor by which the energies of the corrected superclusters have to be multiplied in order to yield an accurate estimation of the particle energy at production vertex. After defining the crystal intercalibration and the cluster energy corrections as described in section 2.2 no remaining correction should be required and this factor should be 1.

2.1 Superclustering

Superclustering algorithms are designed to collect in (super-)clusters a fraction as large and as stable as possible of the shower energy, in particular by recovering energy spread in ϕ due to secondary Bremsstrahlung emission and photon conversions in the material in front of the ECAL. On the other hand, they should also avoid collecting in the same (super-)cluster energy deposits due to different particles, and to minimize the effects of noise fluctuations. The CMS standard superclustering algorithms are: the *Hybrid algorithm* in the barrel region and the *Multi5x5 algorithm* for the endcaps (Refs. [2, 5]).

Local maxima (“seeds”) in energy deposit above some threshold are identified, to which neighboring cells are joint as long as they contain an energy deposit significantly higher than the noise (80 MeV in EB, 300 MeV in EE). Electromagnetic “clusters” are thus formed, which in turn can be associated into “superclusters”.

For the Hybrid algorithm, a list of “seed” crystals with transverse energy above 1 GeV is first constructed. Starting from a seed crystal, a cluster is defined as an ensemble of ϕ -contiguous “dominos” which have collected an energy larger than 100 MeV. Each domino consists of 5 crystals with the same ϕ value, which corresponds to a domino width of 0.087 in η . Valleys, where less than 100 MeV are collected in a domino, separate different clusters. The dominos are then clustered in ϕ , each distinct cluster of dominos being requested to have a seed domino with energy greater than 0.35 GeV. The ϕ roads are allowed to extend up to ± 10 crystals around the seed, which corresponds to ± 0.174 rad.

For the Multi5x5 algorithm, the E_T threshold on seed crystals is 180 MeV. Clusters are formed as 5×5 matrices of crystals centred on the seed crystals; in case of overlaps the overlapping crystals are associated to the cluster with the largest seed E_T . Clusters with an E_T greater than 1 GeV are then eligible as seed clusters for the superclustering. Those clusters, the seed clusters of which are within ± 0.3 radians in ϕ and within ± 0.07 units in η from the seed crystal of the seed cluster, are grouped together.

These algorithms thus differ slightly in the maximum ϕ extension for Bremsstrahlung recovery (± 10 crystals = 0.174 rad for the Hybrid algorithm versus ± 0.3 rad for the Multi5x5 algorithm), and more significantly in the maximum lateral (η) extension of (super-)clusters. For both algorithms, an energy threshold of 4 GeV is requested for a supercluster.

2.2 Intercalibration and energy corrections

The electron/photon energy is computed as the sum of the calibrated signal amplitudes measured in the channels included in the supercluster, corrected as follows:

$$E_{e/\gamma} = f_{5x5}(\eta) \times f_{brem} \times f(\eta, E_T) \times \sum_{cluster} G c_i A_i$$

where the A_i are the amplitudes measured in each crystal in ADC counts, c_i are the crystal intercalibration constants, G defines the crystal scale in MeV/ADC count and $f_{5x5}(\eta)$, f_{brem} and $f(\eta, E_T)$ are supercluster energy correction functions defined further in the text. The crystal scale factor G is defined such that, for unconverted photons in test beam configuration, the $\sum_{cluster} G c_i A_i$ factor in a 5×5 crystal matrix in barrel Module 1 is equal to the unconverted photon energy at vertex.

The intercalibration procedures aim at determining the c_i coefficients. The largest sources of variations are due to the light yield difference between the crystals, and to the VPT gain variations. These variations are reduced by calibration with radioactive sources in the laboratory down to an initial dispersion of 5% for barrel crystals [6] and 7.4% for the endcaps [4]. Then, $\frac{1}{4}$ of the barrel supermodules have been exposed to test beams and intercalibrated to a precision of 0.3%. All the other barrel supermodules have been tested with cosmic rays, the light yield of minimum ionizing muons with quasi-normal incidence in the crystals allowing to intercalibrate them to 1.4%-2.2% [6]. Endcap supercrystals could not be intercalibrated with cosmic rays due to the time constraints of the CMS detector integration.

In-situ intercalibration with collision data will be performed in several steps:

- using the symmetry of the energy deposits in ϕ at each η value. Decomposing the ECAL acceptance into η rings, a precision of 1-3% can be achieved with a few days of collision data [2]. The ultimate precision is limited due to the non-uniformity of the tracker material in ϕ ;
- selecting $\pi^0, \eta \rightarrow \gamma\gamma$ events and constraining the di-photon invariant mass to the known masses of the resonances also allows rapid intercalibration to 1% precision [2].

The $f_{5x5}(\eta)$ function is correcting for the leakage of energy due to crystal staggering in the barrel, which increases with η . This correction was measured in test beams and reproduced accurately with Monte Carlo simulations. It ranges from no correction at $|\eta| = 0$ to 0.7% at $|\eta| = 1.4$ [6] and is applied to all superclusters [6].

The Bremsstrahlung correction is parametrized for several E_T bins as a function of the measured cluster width in the ϕ direction, σ_ϕ . The cluster width in ϕ is an estimation of the amount of energy radiated in the tracker material. This correction is estimated from Monte Carlo simulations. It is expected not to depend much on the precise modelling of the amount of tracker material and its distribution, since it is parametrized as a function of an observable that is correlated with the resulting energy loss (smaller σ_ϕ meaning less material or material concentrated at higher R , hence smaller energy loss).

A determination of the residual electron energy correction $f(\eta, E_T)$ will be performed by constraining the invariant mass of $Z \rightarrow e^+e^-$ events to the known Z boson mass. Due to the convolution of the energy resolution with the Breit-Wigner lineshape of the Z boson, the precision of the determination of the $f(\eta)$ correction function will be about 1%. This determination will be combined with the correction derived from an independent measurement, the E/p ratio of non-radiating electrons from $W \rightarrow e\nu$ decays. For photons, the small difference in energy scale compared to electrons, due to the later development of the EM shower, will at first be corrected using Monte Carlo simulations, then will be measured using final-state radiation photons in $Z \rightarrow \mu^+\mu^-\gamma$. An integrated luminosity of order of 1 fb^{-1} is required for this measurement to be performed.

The energy resolution obtained with barrel supermodules in test beams is shown in Fig. 2 for 120 GeV electrons, before and after all relevant corrections have been applied.

3 Electron reconstruction

Electron candidates are formed by associating an ECAL supercluster to a track reconstructed in the tracker. Two complementary approaches have been developed. In the first approach, the track search is seeded by the supercluster: the initial track segments formed with two hits in the pixel detector layers and/or inner silicon strip detector layers are considered only if they match the supercluster in η and ϕ and in p_T , accounting for the track curvature expected from the supercluster E_T and the four Tesla magnetic field. Both charge hypotheses are considered, and the electron is assumed to originate from the measured beam spot. This approach is well-suited for high- p_T electrons ($p_T > 5 - 10 \text{ GeV}/c$), where the supercluster energy and position estimations are reliable and kinks due to Bremsstrahlung do not impair track reconstruction much [7, 2]. The electron reconstruction efficiency of this approach is shown in Fig. 3.

In the second approach, short track segments with as little as 3 hits reconstructed with the standard tracking algorithm are loosely matched to ECAL deposits in η , ϕ and E_T . To reduce the number of charged pions faking

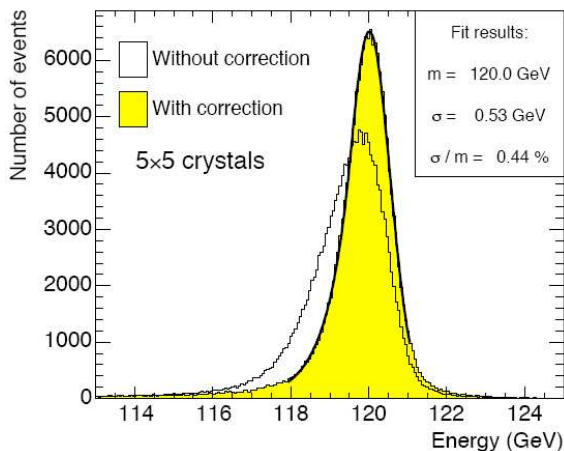


Figure 2: Energy resolution measured with barrel supermodules in a test beam with 120 GeV electrons [1].

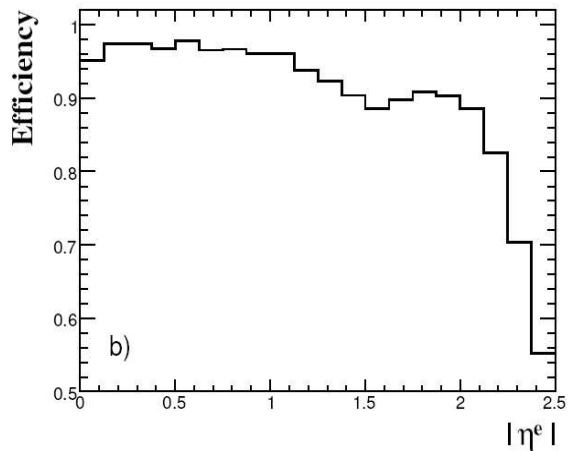


Figure 3: Electron reconstruction efficiency vs. $|\eta|$ for a uniform p_T distribution between 5 and 50 GeV/c [2].

electrons, a pre-identification is performed using a boosted decision tree. The input variables are the ECAL matching variables, preshower information in the endcaps, the number of hits along the trajectory, the track fit χ^2 and an estimation of the Bremsstrahlung energy loss from the difference in the track momentum estimated at the vertex and at the ECAL surface. This approach is expected to be well suited for electrons with $p_T < 5 - 10$ GeV and for non-isolated electrons.

The electron track fit has to account for the higher average energy loss compared to minimum ionizing particles and by the non-Gaussian nature of the Bremsstrahlung energy losses. To account for the latter, a Gaussian-Sum Filter (GSF) has been developed [8] allowing good estimation of the track momentum both at the vertex and at the ECAL surface.

The electron energy is estimated as the average of the supercluster energy and the track momentum weighted by their respective errors, as described in [7]. The supercluster energy contribution dominates for $E_T > 20$ GeV.

4 Electron selection

Jets have a high probability of faking electron candidates by having an electromagnetic energy deposit coincident with a charged particle track. Electron selection aims at purifying the sample of electron candidates, and is conceptually factorized in two aspects:

- **identification**, performed on the basis of the measurements associated to the electron candidate (the ECAL cluster, the HCAL energy behind the ECAL cluster and the trajectory measured in the tracker). Identification is essentially independent of the event topology;
- **isolation**, aiming at selecting isolated primary electrons by requiring little event activity surrounding them.

A set of four robust identification variables have been identified, that are not affected by initial detector miscalibrations and misalignment and can be used at the start of data taking: the differences between the energy-weighted position in (η, ϕ) of the supercluster and the (η, ϕ) of the GSF track at the innermost point extrapolated to the ECAL, the ECAL shower width in the η direction (the direction which is not affected by Bremsstrahlung) and the ratio of the energy measured in the HCAL beyond the ECAL shower to the supercluster energy.

The isolation variables consist of sums of transverse components of energy deposits in ECAL and HCAL and track p_T within conical regions of $\Delta R < 0.4$. The regions are centred on the supercluster position for the calorimetric isolation variables, and on the track direction at the vertex for the track isolation. In all three cases the possible track or energy footprint of the electron is removed by excluding an inner cone, and in the case of the ECAL sum also a narrow strip in the ϕ direction.

The cuts applied on these variables can be optimized in an analysis-dependent way so as to achieve the required signal-to-background ratio. Measurements of the $Z \rightarrow e^+e^-$ and $W \rightarrow e\nu$ cross-sections will provide excellent

benchmark channels to study the performance of electron reconstruction and selection at the start of data taking. About 4000 $Z \rightarrow e^+e^-$ and 40000 $W \rightarrow e\nu$ events are expected after 10 pb^{-1} of data at 10 TeV. The expected spectrum of di-electron events in the $Z \rightarrow e^+e^-$ analysis and the expected \cancel{E}_T spectrum in the $W \rightarrow e\nu$ analysis are shown in Fig. 4 and 5 [9]. In these analyses, the electron selection and p_T cut have been tuned so as to minimize the total cross-section uncertainty (statistical and systematic). In particular a tight selection has been designed that reduces the uncertainty on the $W \rightarrow e\nu$ cross-section due to jet background. The total reconstruction and selection efficiency corresponding to the selections used for the $Z \rightarrow e^+e^-$ analysis is 90% per electron in the ECAL fiducial volume (respectively 75% for the $W \rightarrow e\nu$ analysis) [9].

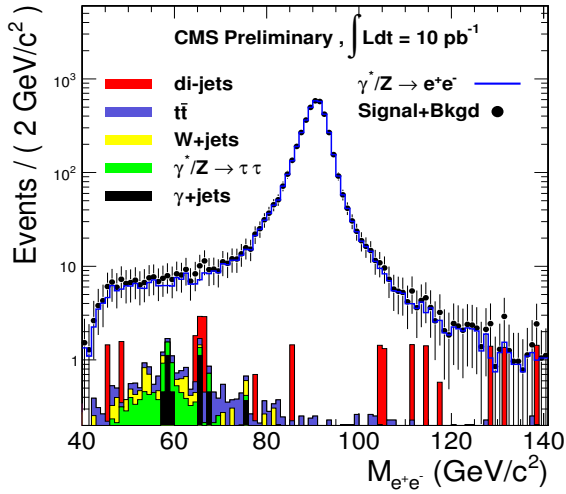


Figure 4: Invariant mass distribution of the pair of selected highest- p_T electrons in the $Z \rightarrow e^+e^-$ analysis [9].

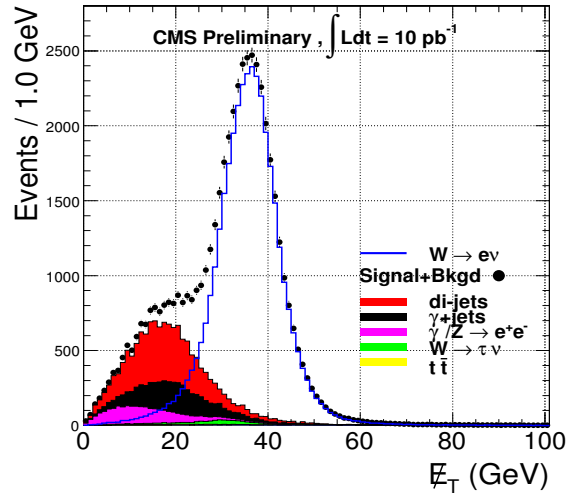


Figure 5: \cancel{E}_T distribution in the $W \rightarrow e\nu$ analysis [9].

5 Photon reconstruction and selection

The main issue in photon energy reconstruction consists in paying special attention to unconverted photons. Optimal energy resolution is expected for these photons, and their contribution to the visibility of the $H \rightarrow \gamma\gamma$ channel is expected to be the largest thanks to the good resolution of the di-photon mass peak [10]. The energy of those photons is measured best using the calibrated energy contained in a 5×5 crystal matrix around the seed crystal, corrected for the lateral leakage correction $f_{5 \times 5}(\eta)$ and for module border effects but otherwise uncorrected. Unconverted photons are identified by means of the R_9 variable, the ratio of the energy contained in a 3×3 crystal matrix to the supercluster energy, which is smaller for unconverted photons.

Photon selection and the rejection of jet background relies on shower shape variables and isolation [11, 12]. To ease photon commissioning at the start of data taking (see section 6) it is advantageous to make use of variables that are expected to have similar distributions for electrons and photons, which can be done by carefully choosing the electron track and energy footprint removal regions.

6 Commissioning of electron and photon reconstruction with data

An essential tool to commission electron reconstruction is the tag-and-probe method [13]. This method relies upon $\gamma/Z \rightarrow e^+e^-$ decays to provide an unbiased, high-purity, electron sample that can be used to measure the efficiency of a particular selection or trigger. Using events passing a single electron trigger, events which contain a well reconstructed electron (the tag) are selected. A second electron, the probe, is selected with criteria leaving it unbiased with respect to the efficiency under study. Purity is ensured by requiring that the invariant mass of the tag and probe electrons is consistent with m_Z . The efficiency is estimated as the fraction of probes passing the

selection criteria under study.

A pure, unbiased sample of photons will only be available after $\sim 1 \text{ fb}^{-1}$ of data from final-state radiation events ($Z \rightarrow l^+l^-\gamma$). The photon selection efficiency can be measured in early data using the tag-and-probe method on $\gamma/Z \rightarrow e^+e^-$ events and applying photon selection criteria to the probe electron. The remaining small differences between electrons and photons can be corrected using Monte Carlo simulations [12].

7 Conclusion

After extensive crystal intercalibration measurements in laboratory and test beams, the CMS electromagnetic calorimeter has been completed with the installation of the endcap Dees in summer 2008 and the installation of the preshower in spring 2009. Intercalibration of $\frac{1}{4}$ of the barrel supermodules was performed in test beams to a precision of 0.3%, while the remaining supermodules have been intercalibrated to about 1.5% in cosmic rays.

With extended periods of data taking with cosmic rays and at full magnetic field performed in 2008, the commissioning of the CMS detector and especially of the ECAL proceeds well. The precision of the crystal intercalibration performed in laboratory was checked from the dE/dx of cosmic rays and with beam dump events. Although the precision of these methods is limited to 1-2% in the barrel and about 10% in the endcaps, the intercalibration was found to be consistent with laboratory measurements and intercalibration in cosmic rays [4]. The temperature and bias voltage stability have been found to match the design requirements. First system tests of the monitoring of the crystal transparency using laser light pulsing delivered encouraging results.

Developments of electron and photon reconstruction and selection algorithms proceed on the basis of simulated data. Commissioning of electron and photon physics objects will rely heavily on the measurement of electroweak processes such as $Z \rightarrow e^+e^-$ events and $W \rightarrow e\nu$.

References

- [1] The CMS Collaboration, *The CMS Experiment at the CERN LHC*, JINST 3:S08004 (2008).
- [2] The CMS Collaboration, *Physics Technical Design Report, Volume 1: Detector Performance and Software*, CERN/LHCC 2006-001 (2006), ISBN 92-9083-268-1.
- [3] The CMS Collaboration, *The Electromagnetic Calorimeter Project Technical Design Report*, CERN/LHCC 97-33 (1997), ISBN 92-90831-122-1.
- [4] The CMS Collaboration, *Crystal ECAL Performance and Operation*, CMS PAPER CFT-09-004.
- [5] E. Meschi, T. Monteiro, C. Seez and P. Vikas, “*Electron Reconstruction in the CMS Electromagnetic Calorimeter*”, CMS NOTE 2001-034.
- [6] The CMS Electromagnetic Calorimeter Group, *Intercalibration of the barrel electromagnetic calorimeter of the CMS experiment at startup*, CMS NOTE 2008/018.
- [7] S.Baffioni et al., *Electron reconstruction in CMS*, CMS NOTE-2006/040.
- [8] W.Adam et al., *Reconstruction of Electrons with the Gaussian-Sum Filter in the CMS Tracker at the LHC*, CMS NOTE-2005/001.
- [9] The CMS Collaboration, *Towards a Measurement of the Inclusive $W \rightarrow e\nu$ and $Z/\gamma \rightarrow e^+e^-$ Cross-Sections in pp Collisions at $\sqrt{s} = 10 \text{ TeV}$* , CMS PAS EWK-09-004.
- [10] The CMS Collaboration, *Physics Technical Design Report, Volume 2: Physics Performance*, J.Phys. G34 (2007) 995-1579, CERN/LHCC 2006-001 (2006), ISBN 92-9083-268-1.
- [11] The CMS Collaboration, *Jet energy calibration with photon+jet events*, CMS PAS JME-09-004.
- [12] The CMS Collaboration, *Data-Driven Background Estimates for SUSY Di-Photon Searches*, CMS PAS SUS-09-004.
- [13] G. Daskalakis et al., *Measuring electron efficiencies at CMS with early data*, CMS PAS EGM-07-001.